

Sunder Neelakantan

Department of Mechanical Engineering and Applied Mechanics, University of Pennsylvania, Philadelphia, PA 19104

Prashant K. Purohit

Department of Mechanical Engineering and Applied Mechanics, University of Pennsylvania, Philadelphia, PA 19104

Saba Pasha¹

Perelman School of Medicine,
University of Pennsylvania,
Philadelphia, PA 19104;
Department of Surgery,
The Children's Hospital of Philadelphia,
Philadelphia, PA 19104
e-mail: pashas@pennmedicine.upenn.edu

A Semi-Analytic Elastic Rod Model of Pediatric Spinal Deformity

The mechanism of the scoliotic curve development in healthy adolescents remains unknown in the field of orthopedic surgery. Variations in the sagittal curvature of the spine are believed to be a leading cause of scoliosis in this patient population. Here, we formulate the mechanics of S-shaped slender elastic rods as a model for pediatric spine under physiological loading. Second, applying inverse mechanics to clinical data of the subtypes of scoliotic spines, with characteristic 3D deformity, we determine the undeformed geometry of the spine before the induction of scoliosis. Our result successfully reproduces the clinical data of the deformed spine under varying loads, confirming that the prescoliotic sagittal curvature of the spine impacts the 3D loading that leads to scoliosis. [DOI: 10.1115/1.4048400]

Keywords: spine, scoliosis, sagittal profile, classification, rod mechanics, reduced-order modeling, pediatric

1 Introduction

The etiology of the adolescent idiopathic scoliosis (AIS) remains largely unknown [1,2]. Several hypotheses have been developed to explain the pathomechanism of AIS development [3,5–8]. Among these hypotheses, the upright alignment of the spine in humans, which impacts the mechanical loading of the spine, is believed to be an important factor in induction of scoliosis [3,9]. The shape of the sagittal curvature of the spine, prior to initiation of spine deformity development, has been shown to be different between the scoliotic and nonscoliotic age, sex matched cohorts [10]. The shape of the sagittal curvature of the spine in prescoliotic patients was believed to make the spine rotationally unstable and lead to scoliosis [3,4,11]. However, as the prescoliotic data on the sagittal profile of this patient population is scarce, an analysis that can determine the physiologically acceptable undeformed shapes of the sagittal spine that can lead to scolioticlike deformation can be valuable for early clinical diagnosis of the curves. Identifying the characteristics of the spinal sagittal curvatures that are prone to scoliotic curve development under a general set of loadings can be used as a risk stratification tool for early diagnosis of the disease.

The sagittal curvature of the spine is believed to have an important role in induction of scoliosis [3,12]. However, the data on the sagittal curvature of the spine prior to curve development is scarce. In a previous study, Pasha showed, using finite element modeling, that an S-shaped elastic rod under bending and torsion can deform into loop or lemniscate shape in the transverse projections only as a function of the curve geometry as seen in Fig. 1 [3]. When those curve geometries were compared to the clinical data, it was observed that sagittal curvature of the scoliotic patients also related to the transverse projection of the curve, in the same manner as an elastic rod [3]. Our strategy to efficiently identify sagittal curvatures of the spine under loads is to analytically model the spine as an elastic rod [3]. Since the spine is a slender structure whose length dimension is much longer than the cross-sectional dimensions we treat it as an elastic rod in this work. This is sufficient for our purposes since we are interested in the shape of the centerline of the spine, not the stresses in the

cross section which are more reliably computed using finite element calculations. For simplicity, we assume that the rod has a circular cross section and is inextensible. A circular rod is the simplest approximation of the shape of the spine cross section. It also has the advantage that the moment—curvature relation is isotropic in the cross section. Inextensibility is a good assumption because a pediatric spine deforms primarily in bending under applied loads, not in uniaxial compression/tension due to its shape. Both these assumptions are introduced for convenience and can be relaxed in a more general theory [13].

Since the material of the spine can be modeled as linearly elastic for small strains [14], our rod model for the spine has two equal bending moduli $K_b(s)$ and a twisting modulus $K_t(s)$ which vary as a function of position s along the centerline of the cross section. The moduli are allowed to vary as a function of position because the cross-sectional dimensions of the spine as well as the material properties of the spine are different depending on the position. For example, the thoracic region has a higher modulus compared to the lumbar region due to attachment of the rib cage. Furthermore, we wanted to allow for the possibility that a scoliotic spine may have these properties varying in a different manner compared to a healthy one. We also assume that the stress-free configuration of our rod model for the spine is S-shaped as observed in a human upright standing position. Thus, our rod has a spontaneous curvature $\kappa_0(s)$ (which is inversely proportional to the radius of curvature) which is a function of position along the centerline. This stress-free curvature is assumed to have zero twist component for a healthy spine. The advantage of modeling the spine as a curved elastic rod under loads is that its deformed shapes can be computed by solving a few ordinary differential equations rather than performing a full finite element calculation which requires many input variables. We show in this paper that our model, although simple, can reproduce many important features in the deformation of spines that have been observed clinically and studied in finite element calculations.

This study aims to determine the deformation patterns of various S-shaped elastic rods as are observed in sagittal curvature of the scoliotic spines. It also aims to match the simulated deformation of such a rod model to the clinical data by altering the mechanical loading and mechanical properties of the rods. We hypothesized that an elastic rod under bending and torsional moments deforms in a similar manner as a pediatric spine with scoliosis. Also, the rod's deformation and clinical data of the

¹Corresponding author.

Manuscript received January 14, 2020; final manuscript received August 19, 2020; published online November 11, 2020. Assoc. Editor: Anton E. Bowden.

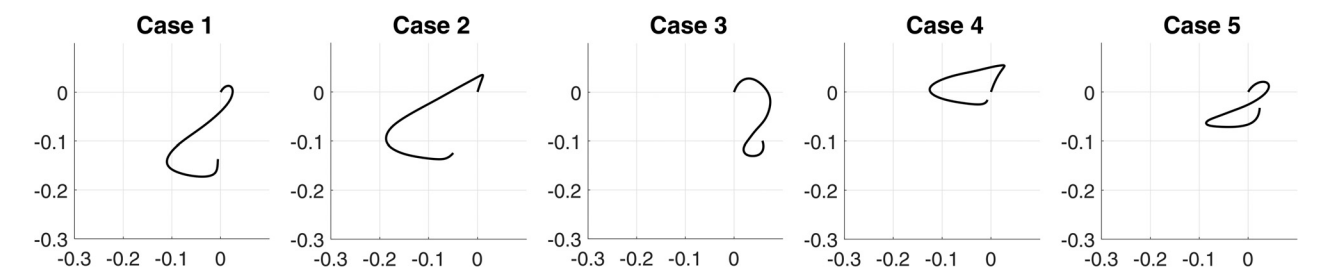


Fig. 1 The transverse view of the five cases of scoliosis

corresponding curved spines can produce similar deformations by altering the mechanical loading of the rods.

2 Methods

2.1 Clinical Data and Data Preparation. The deformed sagittal curvatures of the scoliotic spine were determined from a previous classification study of 103 scoliotic patients [15]. In brief, these 3D curves were generated by postprocessing of the clinical radiographs [16]. A hierarchical clustering determined the subsets of the patients in this cohort with five significantly different 3D spinal curves. The five cases are presented below in Fig. 1. It was shown that these five subtypes can be divided into two groups based on the top-down view (X-Y) of the 3D curves: cases 1, 3, and 5 have lemniscate shaped, also known as figure eight-shaped X–Y view and cases 2 and 4 have loop shaped X–Y view. We used these two patterns (loop and lemniscate) as the basis of our study to describe, using forward and backward mechanics, the parameters causing an undeformed spine to develop either of these deformation patterns. These views are also known as sagittal view (Y–Z view), frontal view (X–Z view), and transverse view (X–Y view).

2.2 Elastic Rod Model. Let us consider the undeformed spine as an S-shaped elastic rod. The sagittal plane of the spine is chosen to be co-incident with the y-z plane of the lab frame. The undeformed rod is assumed to have no out-of-plane curvature with respect to the sagittal plane as would be the case for a healthy spine. The origin of the lab coordinate system $[\mathbf{e}_x \ \mathbf{e}_y \ \mathbf{e}_z]$ is placed at the bottom end of the spine s=0 where s is an arc length coordinate along the centerline of the spine. The position of a point s in the deformed configuration is $\mathbf{r}(s) = x(s)\mathbf{e}_x + y(s)\mathbf{e}_y + z(s)\mathbf{e}_z$.

Now, we define the Frenet frame for the rod, given by the triad $[\hat{\mathbf{t}}(s) \quad \hat{\mathbf{v}}(s) \quad \hat{\boldsymbol{\beta}}(s)]$. Here, $\hat{\mathbf{t}}(s)$ is the tangent vector and is given by the equation $\hat{\mathbf{t}}(s) = (d\mathbf{r}/ds)$. It is a unit vector because the rod is assumed inextensible. The tangent is given by $\hat{\mathbf{t}}(s) = \cos\theta(s)\cos\phi(s)\mathbf{e}_x + \cos\theta(s)\sin\phi(s)\mathbf{e}_y + \sin\theta(s)\mathbf{e}_z$. Here, θ is the polar angle measured from the x-y plane and ϕ is the azimuthal angle used in conventional spherical polar co-ordinates. The conventions and variables are described in Fig. 2. $\hat{\boldsymbol{v}}(s)$ and $\hat{\boldsymbol{\beta}}(s)$ are the normal and binormal vectors, respectively. They are related through the Frenet–Serret equations [17].

The curvature and torsion of the curve describing the centerline of the spine are $\kappa(s)$ and $\tau(s)$, respectively, and are given by

$$\kappa(s) = \sqrt{\theta'^2(s) + \phi'^2(s)\cos^2\theta(s)} \tag{1}$$

$$\tau(s) = \frac{1}{\kappa^2} \left[\left(\theta'' \phi' - \theta' \phi'' \right) \cos \theta + \left(\phi'^3 \cos^2 \theta + 2\theta'^2 \phi' \right) \sin \theta \right]$$
 (2)

2.2.1 Forward Mechanics. This section will deal with the mechanics of the rod. We will present an analytical model to compute the deformed geometry for a given S-shaped rod. The balance of linear momentum [12,18] gives

$$\frac{dn_x}{ds} = 0 (3)$$

$$\frac{dn_{y}}{ds} = 0 (4)$$

$$\frac{dn_z}{ds} + f_z(s) = 0 ag{5}$$

where $\mathbf{n}(s) = [n_x(s) \quad n_y(s) \quad n_z(s)]$ is the force in the rod and the distributed load $\mathbf{f} = f_z(s)\mathbf{e}_z$ is directed only along the \mathbf{e}_z direction due to gravity. It follows immediately from the above that

$$n_x(s) = n_y^0, \quad n_y(s) = n_y^0$$
 (6)

where n_x^0 and n_y^0 are constants that will be determined by the boundary conditions. Since there are no forces applied on the spine along \mathbf{e}_x and \mathbf{e}_y directions, then global equilibrium shows that $n_x^0 = n_y^0 = 0$.

For the balance of angular momentum, the moment in the rod $\mathbf{m}(s)$ is represented in the Frenet frame and given by $\mathbf{m} = m_l \hat{\mathbf{t}} + m_\nu \hat{\mathbf{v}} + m_\beta \hat{\boldsymbol{\beta}}$ at any point. A simple constitutive relation for the moment \mathbf{m} is

$$\mathbf{m} = K_b(s)(\kappa(s) - \kappa^0(s))\hat{\boldsymbol{\beta}} + K_t(s)(\kappa_3(s) - \kappa_3^0(s))\hat{\mathbf{t}}$$
(7)

where $\kappa_3(s)$ is the twist rate and $K_b(s)$ and $K_t(s)$ are the bending and twisting moduli of the spine. We assume that $K_b(s)$ and $K_t(s)$ are functions of s since there is variation in spine stiffness in a scoliotic spine and also because the material properties of the spine may vary as a function of position. $\kappa^0(s)$ and $\kappa^0_3(s)$

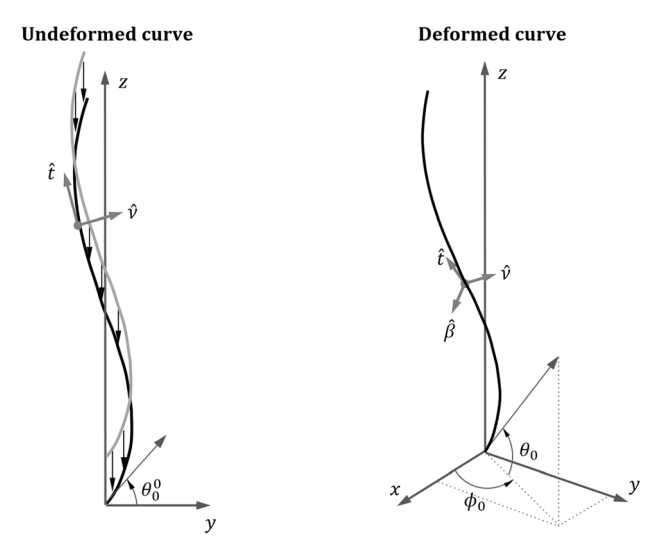


Fig. 2 The centerline of the rod a before and after deformation. The $[x \ y \ z]$ system of cooridnates represent the lab frame. The $[\hat{t} \ \hat{\beta} \ \hat{\nu}]$ system represents the Frenet–Serret frame for the deformed and undeformed configurations.

are the values of the curvatures in the stress free state, respectively. We assume $\kappa_3^0 = 0$. This constitutive law is of the form $\mathbf{m} = K_b(\kappa_1 - \kappa_1^0)\mathbf{d}_1 + K_b(\kappa_2 - \kappa_2^0)\mathbf{d}_2 + K_t(\kappa_3 - \kappa_3^0)\mathbf{d}_3$ where $[\mathbf{d}_1(s) \ \mathbf{d}_2(s) \ \mathbf{d}_3(s)]$ is a material frame that convects with the arc-length coordinate s along the centerline of the cross-section. Now, the derivative of the moment becomes

$$\frac{dm}{ds} = \begin{bmatrix}
\left[\frac{dK_b}{ds}\left(\kappa(s) - \kappa^0(s)\right) + K_b(s)\left(\frac{d\kappa}{ds} - \frac{d\kappa^0}{ds}\right)\right]\hat{\boldsymbol{\beta}} \\
\left[\left(K_t(s)\left(\kappa_3(s) - \kappa_3^0(s)\right) - K_b(s)\tau(s)\left(\kappa(s) - \kappa^0(s)\right)\right]\hat{\boldsymbol{v}} \\
\left[\frac{dK_t}{ds}\left(\kappa_3(s) - \kappa_3^0(s)\right) + K_t(s)\left(\frac{d\kappa_3}{ds} - \frac{d\kappa_3^0}{ds}\right)\right]\hat{\mathbf{t}}
\end{bmatrix}$$

Hence, the conservation of angular momentum boils down to [12,18]

$$\frac{dK_b}{ds} \left\{ \left\{ \kappa(s) - \kappa^0(s) \right\} + \left\{ \left\{ K_b(s) \left(\frac{d\kappa}{ds} - \frac{d\kappa^0}{ds} \right) \right\} + n_\nu = 0 \right\} \right\}$$
 (9)

$$K_t(s)\{\kappa_3(s) - \kappa_3^0(s)\} - K_b(s)\tau(s)\{\kappa(s) - \kappa^0(s)\} - n_\beta = 0$$
 (10)

$$\frac{dK_t}{ds}\left(\kappa_3(s) - \kappa_3^0(s)\right) + K_t(s)\left(\frac{d\kappa_3}{ds} - \frac{d\kappa_3^0}{ds}\right) = 0 \tag{11}$$

We define

$$K_t(s)(\kappa_3(s) - \kappa_3^0(s)) = m_3(s)$$
 (12)

Then, Eq. (11) shows that

$$\frac{dm_3}{ds} = 0\tag{13}$$

Hence, the twisting moment in our rod model is constant along the arc-length. We can also write the conservation of angular momentum in the lab frame as

$$\frac{dm_x}{ds} + n_z \sin\phi \cos\theta - n_y \sin\theta = 0 \tag{14}$$

$$\frac{dm_y}{ds} - n_z \cos\phi \cos\theta + n_x \sin\theta = 0 \tag{15}$$

$$\frac{dm_z}{ds} + n_y \cos\phi \cos\theta - n_x \sin\phi \cos\theta = 0$$
 (16)

If $n_x = n_y = 0$, as we concluded from the balance of linear momentum, then the third equation above gives $m_z = T$, a constant that is determined by a torque boundary condition applied at s = 0.

Finally, the moment–curvature relation is given by

$$\mathbf{m} = K_b(s)(\kappa(s) - \kappa^0(s))\hat{\boldsymbol{\beta}} + m_3\hat{\mathbf{t}}$$
 (17)

We express this moment in the lab frame as

$$m_{x} = K_{b}(s) \frac{\kappa(s) - \kappa^{0}(s)}{\kappa(s)} \left[-\phi' \cos \phi \sin \theta \cos \theta + \theta' \sin \phi \right] + m_{3} \cos \phi \cos \theta$$
(18)

$$m_{y} = K_{b}(s) \frac{\kappa(s) - \kappa^{0}(s)}{\kappa(s)} \left[-\phi' \sin \phi \sin \theta \cos \theta - \theta' \cos \phi \right] + m_{3} \sin \phi \cos \theta$$
(19)

$$m_z = K_b(s) \frac{\kappa(s) - \kappa^0(s)}{\kappa(s)} \phi' \cos^2 \theta + m_3 \sin \theta$$
 (20)

To better understand the effects of moments, we will describe the effect of a constant moment along a single direction on the spine (S-shaped rod). A moment along $\hat{\mathbf{e}_x}$ axis causes the spine to straighten the lumbar curvature and increase the thoracic curvature (leading to kyphosis). A moment along $\hat{\mathbf{e}_y}$ axis would cause a person to tilt side-ways. A moment along $\hat{\mathbf{e}_z}$ would cause the spine to twist to resemble a helix. Going back to the equations for m_x, m_y, m_z above, $K_b(s), \kappa^0(s)$, and $\kappa(s)$ can be eliminated to give

$$m_x \cos \phi + m_y \sin \phi = -m_z \tan \theta + \frac{m_3}{\cos \theta}$$
 (21)

$$(m_x \sin \phi - m_y \cos \phi) \phi' = \frac{m_z - m_3 \sin \theta}{\cos^2 \theta} \theta'$$
 (22)

Equation (21) can then be solved to get

$$\sin \theta = \frac{m_3 m_z \pm P \sqrt{P^2 + m_z^2 - m_3^2}}{P^2 + m_z^2}, \quad P = m_x \cos \phi + m_y \sin \phi$$
(23)

where the solution branch can be determined from the initial value of $\theta(s)$. We can find an expression for $\phi'(s)$ using Eq. (22) and Eq. (1) to get

$$\phi' = \frac{m_z - m_3 \sin \theta}{K_b(s) \cos^2 \theta} \pm \frac{\kappa^0(s)}{\cos \theta} \frac{1}{\sqrt{1 + \cos^2 \theta \frac{\left(m_x \sin \phi - m_y \cos \phi\right)^2}{\left(m_z - m_3 \sin \theta\right)^2}}} \tag{24}$$

where the " \pm " sign is dependent on the sign of $\phi'(s)$.

Finally, the analytic model of the spine is given by the following system of differential-algebraic equations:

$$\frac{dn_z}{ds} = -f_z(s) \tag{25}$$

$$\frac{dm_x}{ds} = -n_z \sin \phi \cos \theta \tag{26}$$

$$\frac{dm_y}{ds} = n_z \cos \phi \cos \theta \tag{27}$$

$$\frac{d\phi}{ds} = \frac{m_z - m_3 \sin \theta}{K_b(s) \cos^2 \theta} \pm \frac{\kappa^0(s)}{\cos \theta} \frac{1}{A}$$
 (28)

$$\theta = \sin^{-1} \left(\frac{m_3 m_z \pm P \sqrt{P^2 + m_z^2 - m_3^2}}{P^2 + m_z^2} \right)$$
 (29)

$$A = \sqrt{1 + \cos^2\theta \frac{\left(m_x \sin\phi - m_y \cos\phi\right)^2}{\left(m_z - m_3 \sin\theta\right)^2}}$$
 (30)

$$P = m_x \cos \phi + m_y \sin \phi \tag{31}$$

$$\frac{dx}{ds} = \cos\phi\cos\theta\tag{32}$$

$$\frac{dy}{ds} = \sin\phi\cos\theta\tag{33}$$

 $^{^2}$ It assumes that the stress-free curvature of the spine is aligned along the binormal vector $\boldsymbol{\beta}(s)$. This is certainly true for planar deformations of a healthy spine for which x(s) = 0 for all s. We show later that it also gives good results for full 3D deformations even though it is not the most general constitutive law.

$$\frac{dz}{ds} = \sin\theta \tag{34}$$

In the above the body force, $f_z(s)$ can be found from a generalized load distribution along the upper body as given by Pasha et al. [19].

2.2.2 Inverse Mechanics. In this section, we will present a method to extract the properties of the undeformed rod and the forces acting on it, given the deformed geometry. The deformed geometry has been obtained from clinical data of patients suffering from scoliosis and is given as a set of position vectors of points along the deformed spine [15]. We interpolate the data to obtain a larger array of points which are spaced uniformly and closer together than the clinical data. The size of the larger array is N (which can be set) and each point be given by $p_i = [x_i \ y_i \ z_i]$, where i goes from 1 to N. Then, the length of the spine can be computed by

$$\Delta p_i = p_{i+1} - p_i, \quad L = \sum_{i=1}^N \sqrt{||\Delta p_i||_2}$$
 (35)

Consider s as an array of N points which can be defined by $s_i = (((i-1)L)/N)$. Hence, we can compute θ and ϕ by

$$\theta_i = \tan^{-1} \left(\frac{\Delta p_{z_i}}{\sqrt{\Delta p_{x_i}^2 + \Delta p_{y_i}^2}} \right) \tag{36}$$

$$\phi_i = \tan^{-1} \left(\frac{\Delta p_{y_i}}{\Delta p_{x_i}} \right) \tag{37}$$

We can then use θ_i and ϕ_i to compute their derivatives with respect to s, i.e., θ_i' and ϕ_i' ; we use these to compute the deformed curvature K_i . Then, we use $f_z(s)$ to determine the moments.

2.2.3 Moment Calculation From Generalized Body Force. Recall the governing system of differential-algebraic equations above, specifically Eqs. (25)–(27). We can compute the values of $m_x(s)$ and $m_y(s)$ since we have values of θ and ϕ . However, we do not know the initial values (at s=0) of the moments. To find $m_x(0)$, $m_y(0)$, m_z and m_3 , we minimize the least squares error between Eq. (29) and the clinical data. This is given by

$$\operatorname{err}(x_1, x_2, x_3, x_4) = \sum_{i=1}^{N} \left[\theta_i - \sin^{-1} \left(\frac{x_4 x_3 \pm P_i \sqrt{P_i^2 + x_3^2 - x_4^2}}{P_i^2 - x_4^2} \right) \right]^2$$
(38)

$$P_i = (m_{x_i} + x_1)\cos(\phi_i) + (m_{y_i} + x_2)\sin(\phi_i)$$
 (39)

$$[m_{x_1}, m_{y_1}, m_z, m_3] = \underset{x_1, x_2, x_3, x_4}{\arg\min} \operatorname{err}(x_1, x_2, x_3, x_4)$$
 (40)

Hence, we offset the m_x and m_y values by m_{x_1} and m_{y_1} , respectively. Now, we use the moment values to determine the $K_b(s)$ and $\kappa^0(s)$. We use Eq. (20) to define an error term based on the least squares method to determine $K_b(s)$ and $\kappa^0(s)$

$$h_i(x_1, x_2) = \left(x_1 \phi_i' \cos^2 \theta_i - \frac{x_2 \phi_i' \cos^2 \theta_i}{\kappa_i} + m_3 \sin \theta_i - m_z\right)^2$$
 (41)

$$[K_{b_i}, K_{b_i} \kappa_i^0] = \arg\min_{x_1, x_2} h_i(x_1, x_2)$$
 (42)

Subject to the condition $K_{b_i} > 0$, $\kappa_i^0 > 0 \quad \forall \quad i \in [1, N]$.

After verifying the values from the minimization, we compute the spinal geometry *prior* to twisting using a special case of the ODEs with $\phi(s) = \pi/2$, implying that $\phi' = 0$. For this case, we assume that the spine is a planar rod being deformed by $f_z(s)$ alone. This leads to out of plane moments going to 0, i.e., $m_v(s) = 0$, $m_z = 0$, $m_3 = 0$ with only $m_x(s)$ being the nonzero

moment. We get the geometry by solving the following differential equations:

$$\frac{dn_z}{ds} = -f_z(s) \tag{43}$$

$$\frac{dm_x}{ds} = -n_z(s)\cos\theta\tag{44}$$

$$\frac{d\theta}{ds} = \frac{m_x}{K_b} + \kappa^0 \tag{45}$$

$$\frac{dy}{ds} = \cos\theta \tag{46}$$

$$\frac{dz}{ds} = \sin\theta \tag{47}$$

with the initial conditions being

$$n_z(0) = n_{z_0} (48)$$

$$m_{x}(0) = 0 \tag{49}$$

$$\theta(0) = \theta_0 \tag{50}$$

$$y(0) = 0 (51)$$

$$z(0) = 0 \tag{52}$$

where n_{z_0} is the weight of the upper body, and θ_0 is the base angle of the spine in the sagittal plane at s = 0.

We presented these curves in Fig. 3. We chose $\kappa^0(s)$ to ensure that the rod remains upright. We constrain the horizontal displacement of the top of the rod to remain under 15% of the vertical displacement. We set this bound to ensure that the head remains roughly over midline of the body in the sagittal plane.

Here, we define a few terms for ease of understanding. We define S as the point of inflection of the rod, i.e., where the curvature approaches 0. K_P is average of the curvature values of the part of rod occupying s < S, i.e., $1/K_P$ is the radius of curvature of the lumbar region of the spine. K_N is the average of the curvature of the part of the rod occupying s > S, i.e., $1/K_N$ is the radius of curvature of the thoracic region of the spine. We present these values in Table 1

$$S = \arg\min_{s} \kappa^{0}(s) \tag{53}$$

$$K_P = \frac{\int_0^S \kappa^0(s) \, \mathrm{d}s}{S} \tag{54}$$

$$K_P = \frac{\int_S^L \kappa^0(s) \, \mathrm{d}s}{L - S} \tag{55}$$

We can see the effects of the moments better in the Frenet frame of the rods. We compute the Frenet frame $(\hat{\mathbf{t}} \quad \hat{\mathbf{v}} \quad \hat{\boldsymbol{\beta}}])$ for the curve prior to the twist (presented in Fig. 3) as

$$\hat{\mathbf{t}} = \cos \theta^0 \, \hat{\mathbf{e}_{\mathbf{v}}} + \sin \theta^0 \, \hat{\mathbf{e}_{\mathbf{z}}} \tag{56}$$

$$\hat{\mathbf{v}} = \sin \theta^0 \, \hat{\mathbf{e}_{\mathbf{v}}} - \cos \theta^0 \, \hat{\mathbf{e}_{\mathbf{z}}} \tag{57}$$

$$\hat{\beta} = \hat{\mathbf{e}_{\mathbf{x}}} \tag{58}$$

where θ^0 is defined in Fig. 2. We then decompose the moments along this frame and plot $m_{\nu}(s)$ on the pretwist curve in Fig. 4. Now, $m_{\beta}(s)$ is responsible for the shape of the spine in the sagittal view while $m_{\nu}(s)$ is responsible for the shape of the spine in the

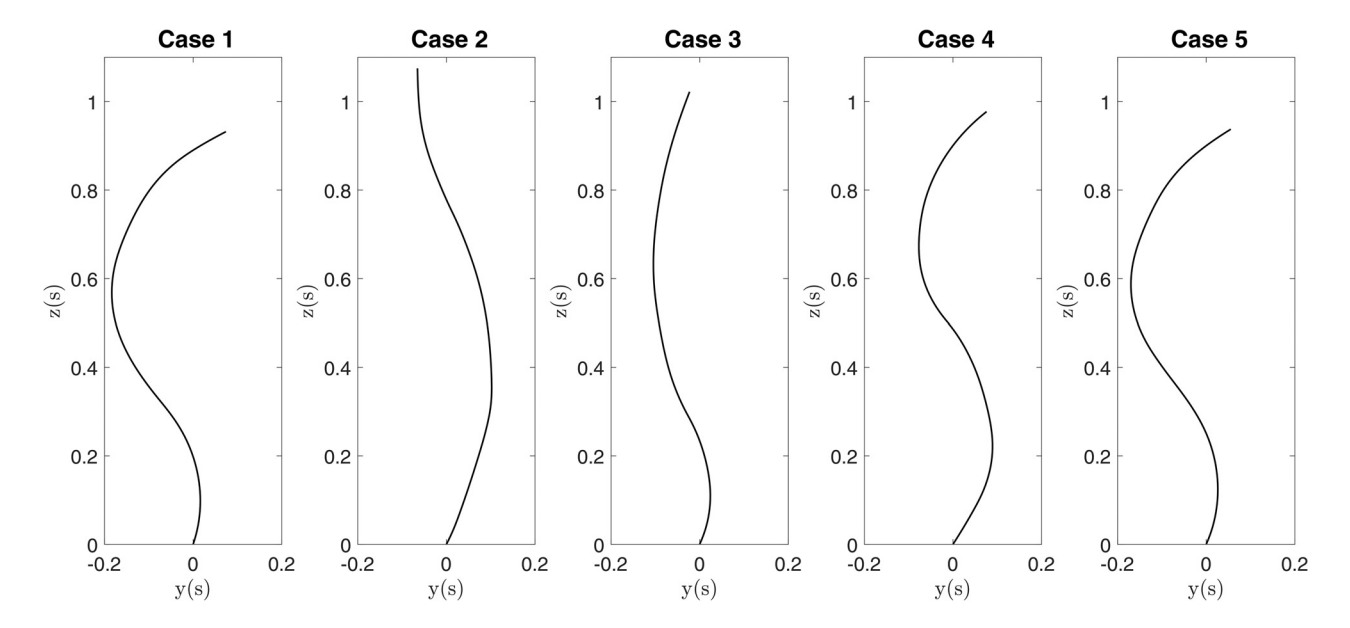


Fig. 3 The geometry of the spine before twist in the sagittal view

Table 1 Table of average curvature values of the thoracic and lumbar regions

| Case | K_P | $\mathbf{K}_{\mathbf{N}}$ | S | θ_{base} (deg) | $M_z \; (\text{N}{\cdot}\text{m})$ | $Max(\mathbf{K_b}) (N \cdot m^2)$ | $Min(\mathbf{K_b}) (N \cdot m^2)$ | R^2 | RMS error (%) |
|--------|-------|---------------------------|------|-----------------------|------------------------------------|-----------------------------------|-----------------------------------|--------|---------------|
| Case 1 | 2.84 | 2.38 | 0.34 | 72.15 | -1.32 | 490.75 | 93.92 | 0.9932 | 6.34 |
| Case 2 | 0.95 | 1.27 | 0.71 | 62.72 | 21.72 | 339.76 | 1.15 | 0.9922 | 8.54 |
| Case 3 | 3 | 0.9 | 0.3 | 66.58 | 16.52 | 771.38 | 3.08 | 0.9931 | 6.64 |
| Case 4 | 2.29 | 2.96 | 0.53 | 53.38 | -25.24 | 732.03 | 1.6 | 0.9917 | 6.35 |
| Case 5 | 2.64 | 2.43 | 0.38 | 66.82 | -24.49 | 433.84 | 65.82 | 0.9926 | 6.13 |

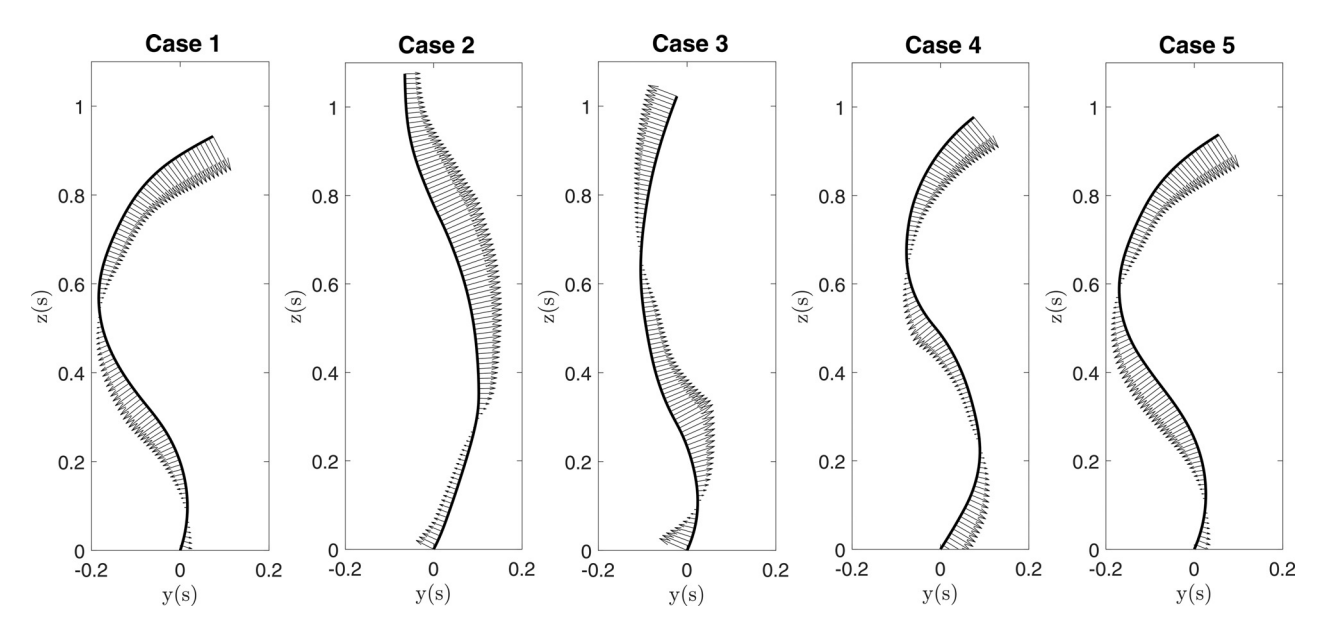


Fig. 4 $m_{\nu}(s)$ plotted on the pretwist curve. Vectors point away from the curve.

frontal view. We will present an explanation using case 5 as an example in Sec. 4.

3 Results

We applied the inverse mechanics method to the five clinically derived cases to determine the stiffness, undeformed curvature, and moments. We validated the model by using the parameters to solve the system ODEs (Eqs. 32–34). We present a comparison between the clinical data and the model in the

transverse view in Fig. 5 and the sagittal view in Fig. 6 and the frontal view in Fig. 7. These figures shows that the model is in good agreement with clinical data quantified by the RMS error in Table 1. We see a mean RMS error of 6.8% with a maximum RMS error of 8.54% for case 2. Plots of $m_x(s)$ and $m_y(s)$ are presented in Fig. 8. The moment and stiffness values of the spine are presented in Table 1. We used these model parameters to predict the curvature using Eq. (42). The shapes of the spine prior to the twisting effects for each of the cases in Fig. 1 are presented in Fig. 3.

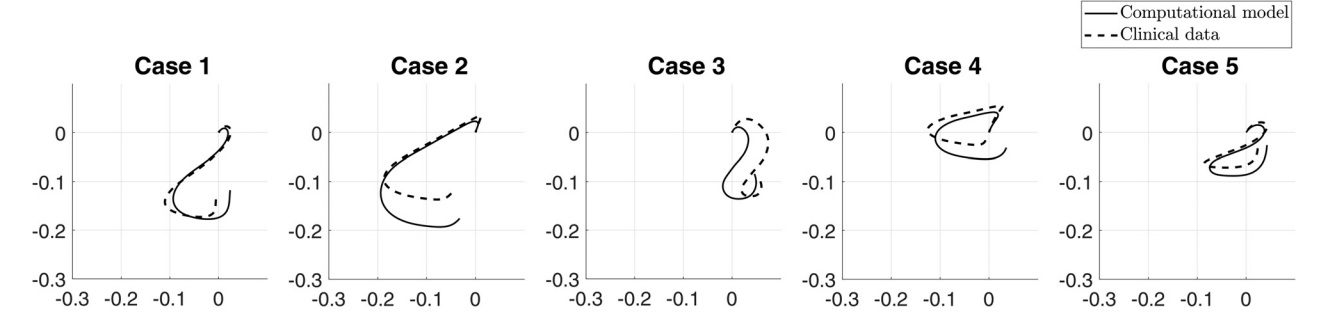


Fig. 5 Comparison between the clinical data and the computational model in the transverse view. The solid lines are the results of the computational model. The dotted lines are clinical data from Ref. [15].

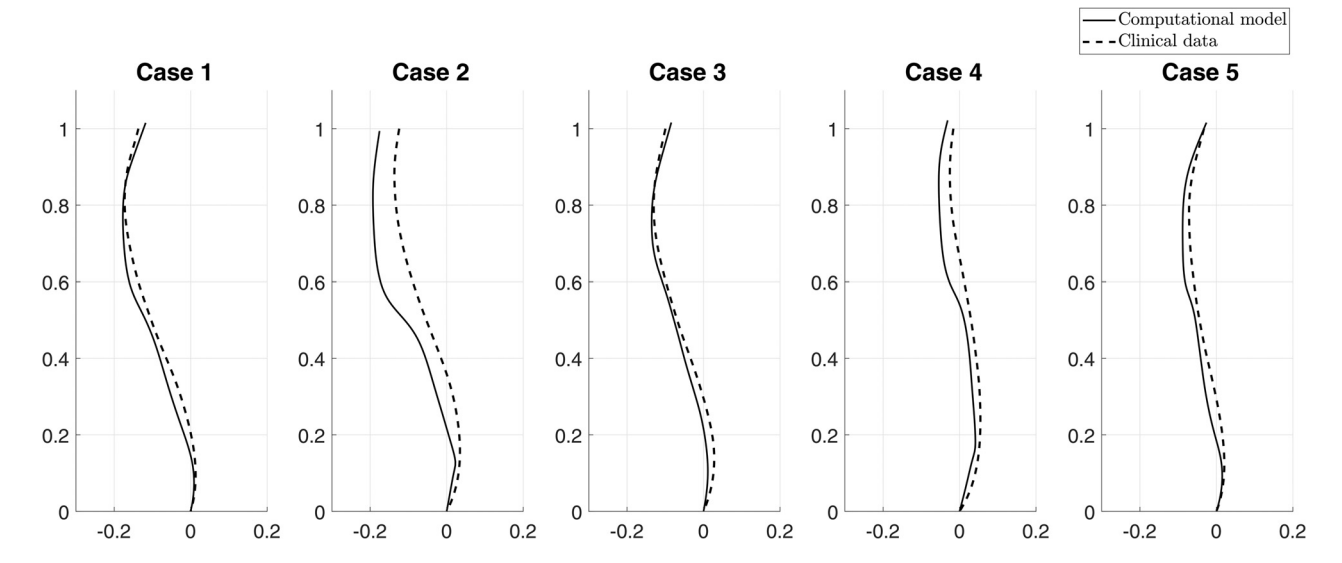


Fig. 6 Comparison between the clinical data and the computational model in the sagittal view. The solid lines are the results of the computational model. The dotted lines are clinical data from Ref. [15].

We present the curve prior to twist and the $m_{\nu}(s)$ component of the moment decomposed along the Frenet frame for the curves presented in Fig. 4 to better understand the physical significance of the moments and the effect they have on the deformed shape in the transverse view.

We compute the average curvatures for the two parts of the S-shaped rod and the point of inflection and present them in Table 1. The m_z experienced in each case along with the variation in stiffness is also presented in Table 1. We also present a representative stiffness curve for this model in Fig. 9 (taken from case 5).

4 Discussion

The enigmatic spinal deformation in adolescents has been studied for centuries. Here, we use an analytical model of a curved elastic rod to study the fundamentals of the 3D deformations as it relates to the curve development in scoliosis. We use the clinical subgroups of scoliotic patients with a thoracic curve, determined from a 3D classification of the spine [15], and apply inverse mechanics to determine the undeformed shape of the spine. In this analysis, by *untwisting* the S-shaped rod under gravity, we determine the shape of the spine before the induction of scoliosis. Our results show the characteristic of the S-shaped curvatures, i.e., sagittal profile of the spine, was preserved after untwisting the curve, meaning that in the spines with a loop shaped projection (cases 2 and 4) the length of the spinal section with a lordotic curve is longer than the length of the spine with a kyphotic curve

with an inflection point above the center of spinal sagittal curve, whereas spines with a lemniscate transverse projection (cases 1, 3, and 5) have a slightly larger kyphosis than lordosis with an inflection point below the center of the curve. We compared the deformed S-shaped curves under gravity and torsion to the clinical data and found acceptable agreement between the simulations and clinically reported deformity patterns as seen in Figs. 5 and 6.

Pasha showed that scoliotic spine can be modeled as an elastic rod under bending and torsion [3]. Such reduced-order model showed that an S-shaped rod deforms into loop or lemniscate shapes in the transverse projection only as a function of the curve geometry as seen in Fig. 1 [3]. When those curve geometries were compared to the clinical data, it was observed that sagittal curvature of the scoliotic patients also related to the transverse projection of the curve in the same manner as an elastic rod [3]. However, as that study used the sagittal profile of the scoliotic curves, it could not be shown what characteristics of the sagittal plane determined the deformity patterns of the spine in scoliosis. Our analysis in this paper uses defined scoliotic curve types and applies inverse mechanics analysis to determine the prescoliotic shape of the spine. These shapes are then shown to produce the 3D scoliotic deformity, under physiologically acceptable conditions, that matches the clinical data. The current analysis shows that the moments that cause the off-plane curve deformation can be formulated as a function of the curve's sagittal parameters as seen in Fig. 4. This study explains how the initial sagittal curvature of the spine impacts the mechanical loading of the spine,

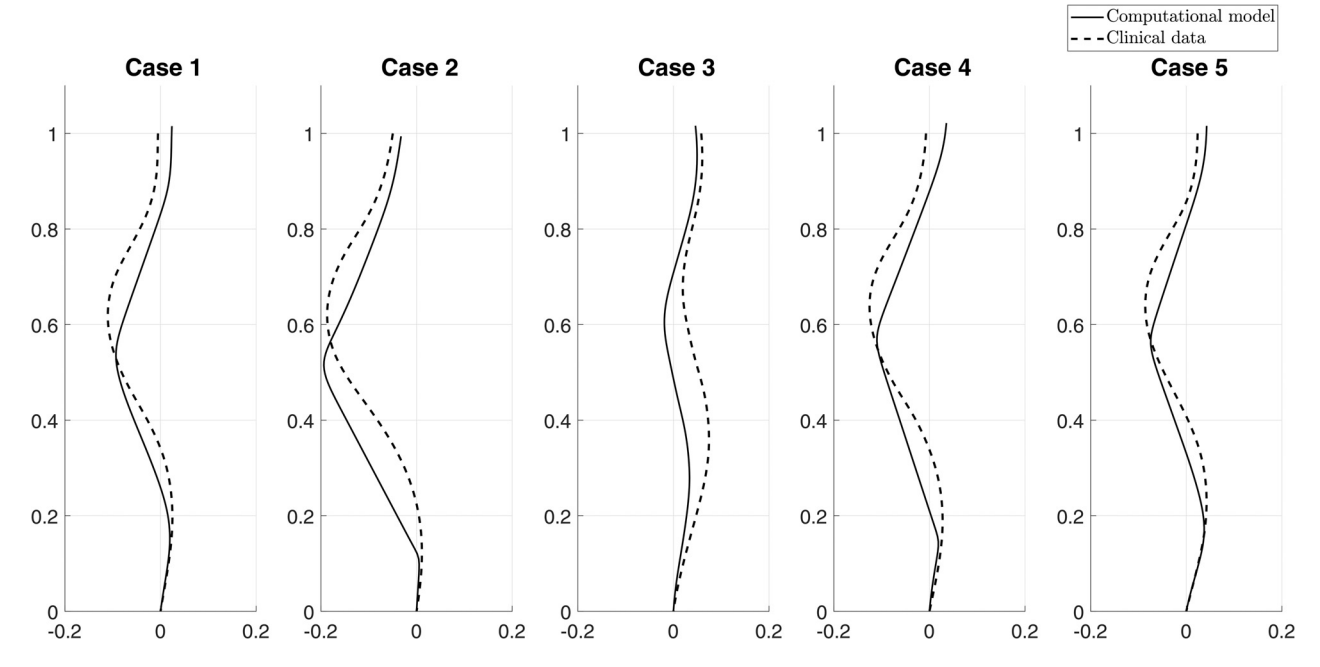


Fig. 7 Comparison between the clinical data and the computational model in the frontal view. The solid lines are the results of the computational model. The dotted lines are clinical data from Ref. [15].

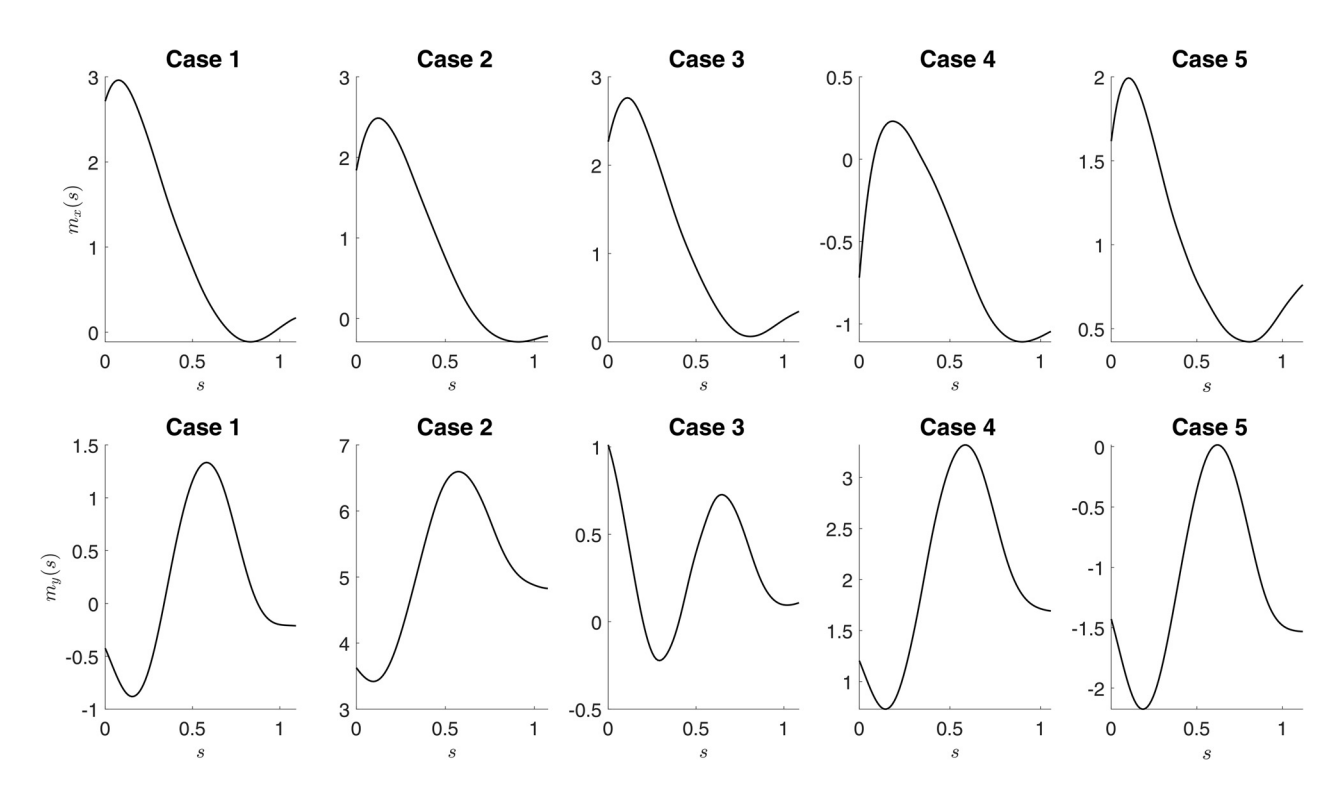


Fig. 8 Trends of $m_x(s)$ and $m_y(s)$ for the five cases. The plots in the top row correspond to the $m_x(s)$ values for the five cases. The plots in the bottom row correspond to $m_y(s)$.

which in turn leads to the scoliotic like deformation. Understanding the fundamentals of the spinal loading and resultant deformities is the first step in developing clinical methods that prevent or reverse the deformity development.

While several hypothesis have been developed to explain the spinal deformity in AIS, the use of analytical models remains unexplored. The only other existing analytical model of the spine for scoliosis explains this deformity only in one plane (frontal

plane). This model considers the spine as a 2D straight rod, thus ignoring the curvature of the spine in the sagittal plane. The deformity under gravity then was explained as 2D buckling of the rod. The deformation modes in the frontal plane were used to explain variations in the curve types in scoliotic patients [20–22]. But, AIS as we know it, is not 2D buckling. The curve deforms in 3D gradually. Our elastic rod model, as shown in this study, agrees with the characteristics of spinal deformity development in

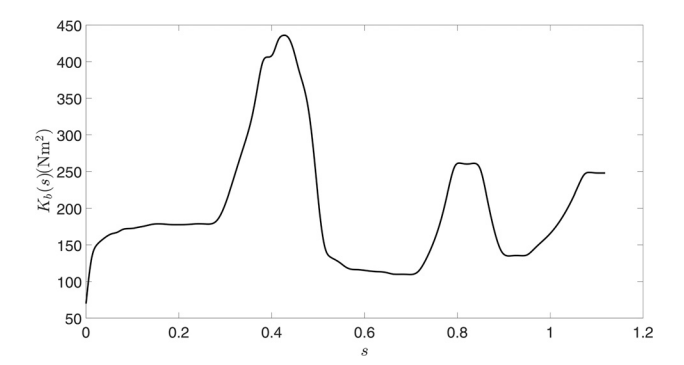


Fig. 9 A representative $K_b(s)$ curve. This is produced from case 5.

scoliosis as it incorporates the variation in the sagittal curvature. Such a deformation may be reversible if all deformations are elastic. The deformation of an elastic rod model, as described here, relates to the deformity patterns of the AIS patients [3,4].

In the current model, in addition to gravity we used a transverse moment to obtain the scoliotic shapes. This moment in the system was originally meant to break the symmetry of the system that would be otherwise only under gravity loads and thus would not deform in 3D. This torsion can be physiologically justified by the trunk mass asymmetry [12,23,24]. There is no evidence that this moment (torsion) is larger in scoliotic patients than in nonscoliotic patients or whether this moment varies between different curve types as a result of differences in the kyphosis and the chest volume. We stipulate that such torsion may also be caused by a period of fast growth in the spine; however, the trunk mass asymmetry may dictate the direction of 3D deformation resulted from the growth. This factor merits investigation to further personalize the model.

We used several filtering criteria as the solution set to the inverse problem is not unique. We eliminated solutions that are physiologically not reasonable. We limited the maximum possible m_z and $K_b(s)$. We also ensured that the characteristic of the curve in the sagittal view was preserved. If one or more of these limiting conditions were not met, we repeated the optimization procedure with different initial values. This shows us that while the shape of the curve in the sagittal view is important in the induction of scoliosis, a unique curve cannot be produced given a deformed shape. We can determine a set of possible solutions with reasonable physiological parameters for a given deformed shape and can present a unique solution given more clinical data.

The spikes in $K_b(s)$ and $\kappa^0(s)$ are filtered out to ensure that functions and their derivatives do not have discontinuities. The comparison between the clinical data and the solution from the model is presented in the results section. The solutions to Eq. (39) and Eq. (41) are not unique. The minimization function finds the local minima of the function in the neighborhood of the starting point. We select solutions by changing the starting point. We selected the solutions based on physiological limitations, which we explain in Sec. 4.

We limit our $K_b(s)$ values to 1000 N·m² based on a previous finite element simulations where they modeled the spine as a rod with a circular cross section [3]. We present the maximum and minimum values of $K_b(s)$ for the five cases in Table 1. The $K_b(s)$ (a representative curve is presented in Fig. 9) curve contains three distinct peaks. The peaks in $K_b(s)$ correspond to the peaks in the load function $f_z(s)$. As we simplified the load along the spine to point load with spikes to present the weight of the head and arms K_b showed maximum value at the same points. In reality, it is expected as the loads are distributed more gradually $K_b(s)$ will show a more smooth transition from region-to-region.

We also presented the corresponding $m_x(s)$ and $m_y(s)$ values in Fig. 8. We can see that $m_x(s)$ are always positive for the

lemniscate shapes while they change signs for the loop shapes. Looking at the $m_v(s)$ values, we see that $m_v(s)$ values always stay positive for the loop shape cases. This can be used as a criterion to determine whether loop or lemniscate shapes will develop. We also present plot of $m_{\nu}(s)$ vectors plotted along the undeformed curve to understand the deformation in the X–Z plane. We do not consider the effects of $m_t(s)$ and $m_{\beta}(s)$ as they are responsible for twist and Y-Z plane deformations, respectively. We can see in case 5 in Fig. 4 that $m_{\nu}(s)$ points toward the right—front of spine—at the bottom and top regions and toward the leftbackward—in the middle region and zero at the apices, but for cases 2 and 3 this relationship is reversed since the m_7 was in opposite direction. This direction also relates to the θ which is less than 90 deg at bottom and top and exceeding 90 deg in the middle and 90 deg at the apices. We assume that the base is fixed, hence due to the moment, the curve would deflect toward the positive xaxis in the bottom and top regions. The curve would deflect towards the negative x-axis in the middle region. This is exactly what we see in Fig. 7 for case 5. Hence, we can predict the frontal view after we look at $m_{\nu}(s)$ and since we know that the sagittal curve characteristic is roughly preserved, we can predict the shape of the curve in the X-Y projection.

The current model has several limitations that were required for constructing the analytical solution. First, the rod was considered to be inextensible. The changes in the sagittal alignment of the spine during the course of scoliotic development impacts the disc morphology as a function of mechanical loading and changes the curvature of the spine before any bony deformation occurs [25–27]. This mechanism may extend sections of the spine and contract the adjacent parts. Second, we considered the base angle as the tangent to the curve at the lowest vertebral level. While in reality the alignment of sacrum, which can be aligned independent from the shape of the spine at the lowest vertebral level, plays an important role in regulating the spinal alignment over the femoral heads and transferring the force between the spine and lower extremities [19,28]. Considering the position of the spine over the sacrum may have required additional coordinate system transfer particularly in cases with large sacral slope.

Despite the limitations mentioned above, our model delivers results which are in good agreement with clinical data. The model uses only five variables that can be easily captured in a clinical setup for patient assessment. We can calculate the forces and material properties using the x, y, z co-ordinates and the body force acting on the spine which are easily measurable. This model is advantageous compared to the reduced-order finite element model to study deformation patterns in AIS because it captures the essence of the deformation in an S shaped rod and provides insight into the specifics of the geometrical variables of the sagittal curvature and the deformation patterns.

Acknowledgment

SN and PKP acknowledge partial support through an NSF grant NSF CMMI 1662101.

Funding Data

• National Science Foundation (Grant No. NSF CMMI 1662101; Funder ID: 10.13039/100000001).

References

- Weinstein, S. L., Dolan, L. A., Cheng, J. C., Danielsson, A., and Morcuende, J. A., 2008, "Adolescent Idiopathic Scoliosis," Lancet, 371(9623), pp. 1527–1537.
- [2] Cheng, J. C., Castelein, R. M., Chu, W. C., Danielsson, A. J., Dobbs, M. B., Grivas, T. B., Gurnett, C. A., Luk, K. D., Moreau, A., Newton, P. O., Stokes, I. A., Weinstein, S. L., and Burwell, R. G., 2015, "Adolescent Idiopathic Scoliosis," Nat. Rev. Disease Primers, 1(1), p. 15030.

- [3] Pasha, S., 2019, "3D Deformation Patterns of s Shaped Elastic Rods as a Pathogenesis Model for Spinal Deformity in Adolescent Idiopathic Scoliosis," Sci. Rep., 9(1), p. 16485.
- [4] Pasha, S., 2020, What causes different coronal curve patterns in idiopathic scoliosis? bioRxiv
- [5] Liu, Z., Tam, E. M. S., Sun, G.-Q., Lam, T.-P., Zhu, Z.-Z., Sun, X., Lee, K.-M., Ng, T.-B., Qiu, Y., Cheng, J. C. Y., and Yeung, H.-Y., 2012, "Abnormal Leptin Bioavailability in Adolescent Idiopathic Scoliosis: An Important New Finding," Spine, 37(7), pp. 599-604.
- [6] Gu, S.-X., Wang, C.-F., Zhao, Y.-C., Zhu, X.-D., and Li, M., 2009, "Abnormal Ossification as a Cause the Progression of Adolescent Idiopathic Scoliosis," Medical Hypotheses, 72(4), pp. 416-417.
- [7] Burwell, R. G., 2003, "Aetiology of Idiopathic Scoliosis: Current Concepts," Pediatric Rehabilitation, 6(3–4), pp. 137–170.
- [8] Chu, W. C., Lam, W. M., Ng, B. K., Tze-Ping, L., Lee, K.-M., Guo, X., Cheng, J. C., Burwell, R. G., Dangerfield, P. H., and Jaspan, T., 2008, "Relative Shortening and Functional Tethering of Spinal Cord in Adolescent Scoliosis-Result of Asynchronous Neuro-Osseous Growth, Summary of an Electronic Focus Group Debate of the IBSE," Scoliosis, 3(1), p. 8.
- Castelein, R. M., van Dieen, J. H., and Smit, T. H., 2005, "The Role of Dorsal Shear Forces in the Pathogenesis of Adolescent Idiopathic Scoliosis-a Hypothesis," Med. Hypotheses, 65(3), pp. 501-508.
- [10] Schlösser, T. P., Shah, S. A., Reichard, S. J., Rogers, K., Vincken, K. L., and Castelein, R. M., 2014, "Differences in Early Sagittal Plane Alignment Between Thoracic and Lumbar Adolescent Idiopathic Scoliosis," Spine J., 14(2), pp. 282-290.
- [11] Castelein, R. M., and Veraart, B., 1992, "Idiopathic Scoliosis: Prognostic Value of the Profile," Eur. Spine J., 1(3), pp. 167–169.
- [12] Kouwenhoven, J.-W. M., Vincken, K. L., Bartels, L. W., and Castelein, R. M., 2006, "Analysis of Preexistent Vertebral Rotation in the Normal Spine," Spine, **31**(13), pp. 1467–1472.
- [13] Antman, S., 2006, Nonlinear Problems of Elasticity. Applied Mathematical Sciences, Springer, New York.
- [14] Gibson, L. J., and Ashby, M. F., 1997, Cellular Solids: Structure and Properties (Cambridge Solid State Science Series), 2nd ed., Cambridge University Press, Cambridge, UK.
- [15] Pasha, S., Hassanzadeh, P., Ecker, M., and Ho, V., 2019, "A Hierarchical Classification of Adolescent Idiopathic Scoliosis: Identifying the Distinguishing Features in 3d Spinal Deformities," Plos One, **14**(3), p. e0213406.
- [16] Pasha, S., Schlösser, T., Zhu, X., Mellor, X., Castelein, R., and Flynn, J., 2019c, "Application of Low-Dose Stereoradiography in In Vivo Vertebral

- Morphologic Measurements: Comparison With Computed Tomography," J. Pediatric Orthop., 39(9), pp. 487–494.
- [17] Nizette, M., and Goriely, A., 1999, "Towards a Classification of Euler-Kirchhoff Filaments," J. Math. Phys., 40(6), pp. 2830–2866.
- [18] Audoly, B., and Pomeau, Y., 2010, Elasticity and Geometry: From Hair Curls to the Non-Linear Response of Shells, OUP, Oxford, UK.
- [19] Pasha, S., Aubin, C.-E., Parent, S., Labelle, H., and Mac-Thiong, J.-M., 2014, "Biomechanical Loading of the Sacrum in Adolescent Idiopathic Scoliosis," Clin. Biomech., 29(3), pp. 296–303.
 [20] Lucas, D. B., 1970, "Mechanics of the Spine," Bull. Hospital Jt. Diseases
- Orthopaedic Inst., **31**(2), pp. 115–131.
- [21] Belytschko, T., Andriacchi, T., Schultz, A., and Galante, J., 1973, "Analog Studies of Forces in the Human Spine: Computational Techniques," J. Biomech., 6(4), pp. 361-371.
- [22] Meakin, J. R., Hukins, D. W. L., and Aspden, R. M., 1996, "Euler Buckling as a Model for the Curvature and Flexion of the Human Lumbar Spine," Proc. R. Soc. London. Ser. B: Biol. Sci., 263(1375), pp. 1383-1387.
- [23] de Reuver, S., Brink, R. C., Homans, J. F., Kruyt, M. C., van Stralen, M., Schlösser, T. P. C., and Castelein, R. M., 2019, "The Changing Position of the Center of Mass of the Thorax During Growth in Relation to Pre-Existent Vertebral Rotation," Spine, 44(10), pp. 679-684.
- [24] Janssen, M. M. A., Kouwenhoven, J.-W. M., Schlösser, T. P. C., Viergever, M. A., Bartels, L. W., Castelein, R. M., and Vincken, K. L., 2011, "Analysis of Preexistent Vertebral Rotation in the Normal Infantile, Juvenile, and Adolescent Spine," Spine, 36(7), p. 14.
- [25] Pasha, S., Sankar, W. N., and Castelein, R. M., 2019b, "The Link Between the 3d Spino-Pelvic Alignment and Vertebral Body Morphology in Adolescent Idiopathic Scoliosis," Spine Deformity, 7(1), pp. 53–59.
- [26] Brink, R. C., Schlösser, T. P., van Stralen, M., Vincken, K. L., Kruyt, M. C., Hui, S. C., Viergever, M. A., Chu, W. C., Cheng, J. C., and Castelein, R. M., 2018, "Anterior-Posterior Length Discrepancy of the Spinal Column in Adolescent Idiopathic Scoliosis-a 3d ct Study," Spine J., 18(12), pp. 2259-2265.
- [27] Pasha, S., Smith, L., and Sankar, W. N., 2019d, "Bone Remodeling and Disc Morphology in the Distal Unfused Spine After Spinal Fusion in Adolescent Idiopathic Scoliosis," Spine Deformity, **7**(5), pp. 746–753.
- Jiang, Y., Nagasaki, S., You, M., and Zhou, J., 2008, "Dynamic Studies on Human Body Sway by Using a Simple Model With Special -Concerns on the Pelvic and Muscle Roles," Asian J. Control, 8(3), pp.